Effect of Halogenation on the Energetics of Pure and Mixed Phases in Model Organic Semiconductors Composed of Anthradithiophene Derivatives and C_{60}

Ashkan Abtahi,[†,‡] Samuel M. Mazza,[‡,§] Sean M. Ryno,[‡,§] E. Kirkbride Loya,[‡,§] Ruipeng Li,[∥] Sean R. Parkin,[‡] Chad Risko,[‡,§] John E. Anthony,[‡,§] and Kenneth R. Graham[‡,*]

[†]Department of Physics and Astronomy and [‡]Department of Chemistry, University of Kentucky, Lexington, Kentucky 40506, United States

[§]Center of Applied Energy Research, University of Kentucky, Lexington, Kentucky 40511, United States

[∥]Cornell High Energy Synchrotron Source, Cornell University, Ithaca, New York 14853, United States

S Supporting Information

ABSTRACT: Halogenation, particularly fluorination, is commonly used to manipulate the energetics, stability, and morphology of organic semiconductors. In the case of organic photovoltaics (OPVs), fluorination of electron donor molecules or polymers at appropriate positions can lead to improved performance. In this contribution, we use ultraviolet photoelectron spectroscopy, external quantum efficiency measurements of charge-transfer (CT) states, and density functional theory calculations to systematically investigate the effects of halogenation on the bulk solid-state energetics of model anthradithiophene (ADT) materials, their interfacial energetics with C_{60}, and the energetics of various $ADT:C_{60}$ blend compositions. In agreement with previous work, nonhalogenated ADT molecules show higher energy CT states in blends with C_{60} and lower energy CT states in the ADT/C_{60} bilayers. However, this trend is reversed in the halogenated ADT/C_{60} systems, wherein the CT state energies of $ADT:C_{60}$ blends are lower than those in the bilayers. In bulk-heterojunction photovoltaics, the lower energy CT states present in the mixed phase with the halogenated ADT derivatives will likely decrease the probability of charge separation and increase charge recombination. The less favorable energy landscapes observed upon halogenation suggest that the benefits of fluorination observed in many OPV material systems may be more due to morphological factors.
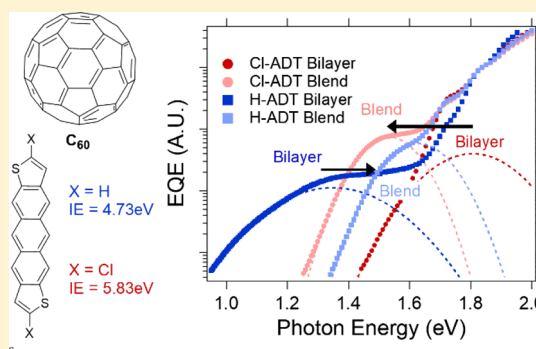
INTRODUCTION

Organic photovoltaics (OPVs) present a promising means to harvest solar energy through lightweight, flexible, portable, and environmentally friendly modules. The record power conversion efficiency (PCE) of OPVs has increased from 5 to 13% over the last decade,[1,2] yet further gains are necessary to enable widespread deployment. As record PCEs have seemingly plateaued,[2] despite considerable research effort, the largely Edisonian approaches employed thus far appear unlikely to enable further appreciable gains. Rather, more fundamental molecular and morphological design principles must be discovered and utilized. One molecular design strategy that has led to higher efficiencies in bulk-heterojunction (BHJ) OPVs is the replacement of select hydrogen atoms on the electron donor molecules or polymers with fluorine atoms.[3−13] Given the widely observed beneficial effects of fluorination, it is important to identify the underlying mechanisms behind device performance improvements to further advance the design of OPV materials.

Fluorination influences many properties across varying length scales that help determine the performance of an OPV material system, from molecular orbital energies through material morphology and topology to OPV-specific device properties.[3,5,10,12,14−28] One of the primary motivations for fluorination of donor polymers in OPVs is to alter the ionization energy (IE) and thereby influence the open-circuit voltage.[13,27−29] From a morphological point of view, fluorination of donor polymers can improve phase purity in the BHJ film and promote the formation of crystalline polymer regions.[15] Fluorination at appropriate positions can also increase the planarity of π-conjugated polymer backbones and alter intermolecular packing,[3,5,16,17,26] which can lead to higher charge-carrier mobilities. In one report, Tumbleston et al. suggested that fluorination alters the molecular orientations and associated intermolecular interactions between polymers and fullerenes from edge-on with the nonfluorinated polymers to face-on with fluorinated polymers.[19] Such changes in the intermolecular interactions at the donor−acceptor (D−A)

interface are likely to impact the energy landscape that is critical to photocurrent generation, including the processes of charge separation and recombination. Here, the energy landscape refers primarily to the relative energies of holes and electrons (i.e., sites) at and away from D−A interfaces. Additionally, fluorination will affect intramolecular ground- and excited-state dipoles. For example, Carsten et al. reported an increase in OPV performance as the difference between the ground- and excited-state dipole moments of the donor polymer repeat unit increased due to fluorination at selected positions.[12,25]

The critical processes of charge separation and recombination occur primarily at interfaces between electron donor and electron acceptor molecules or polymers; therefore, changes in intermolecular interactions and the energy landscape that arise from fluorination are expected to influence the probability of charge separation, charge recombination dynamics, and the performance of the OPV material system. In a BHJ system, the energy landscape will include the site energies for holes and electrons within pure D or A phases, at interfaces between pure D and A phases, and in mixed phases of D and A. Beneficial energy landscapes for promoting charge separation and reducing charge recombination would have lower energy states for holes and electrons within the pure D and A phases and higher energy states for holes and electrons at D−A interfaces or in D−A mixed phases; thus, a thermodynamic driving force would exist for interfacial charge-transfer (CT) states to separate. Charge separation also appears to be more efficient at interfaces between pure D and A phases;[30−32] thus, it should be advantageous when the lowest energy CT states occur between these pure phases as opposed to in mixed D−A phases. Given the importance of the D−A interfacial energy landscape, there is a rapidly growing body of experimental and theoretical work investigating the impact of D−A interfacial energetics on charge separation and PV performance[22,33−35] and how these energetics are determined at the molecular level.[35−46] In this paper, we show how fluorination and chlorination of model anthradithiophene (X-ADT) derivatives impact the energy landscape at planar D−A interfaces and in mixed phases of varying D and A composition, where C_{60} is used as the acceptor. We view this contribution as a step in determining if changes in energy landscapes upon fluorination are a primary factor for many of the observed increases in OPV performance.

Several theoretical models have been employed to investigate the influence of the interfacial energy landscape on charge separation and recombination in OPVs.[22,33,34,38,42] Many of these studies find that changes in the interfacial energy landscape partly account for how charge separation can be so efficient in OPV materials. For example, kinetic Monte Carlo simulations show that the probability of charge separation depends heavily on the D−A interfacial energy landscape,[22,33,34] with interfacial energy offsets of 150−300 milli-electron volts (meV) being necessary to explain the high internal quantum efficiencies observed in some OPV materials. Experimentally, cascade energy landscapes have been created in an effort to promote charge separation and minimize charge recombination, with decreased charge recombination leading to higher V_{OC} values.[34,47−49] More recently, ultrafast spectroscopic measurements show that the migration of holes from higher to lower energy sites can occur within about 100 fs of excitation.[50] These ultrafast spectroscopy measurements suggest that in BHJ OPVs with optimized morphologies, charge separation is in part driven by the migration of holes from higher energy states

at D−A interfaces into lower-energy sites within pure D phases.[50] The combined theoretical and experimental lines of evidence suggest that energetics at interfaces and within phases of varying composition play a key role in driving charge separation in OPV devices.

In addition to the work on energy cascades, there is an increasingly large body of work on the effects of intermolecular interactions, packing arrangements, and morphology on the energy landscape. Theoretical works have used a wide variety of methods,[36] including microelectrostatic simulations,[37,38,42] density functional theory (DFT) calculations,[39−42,51,52] and Green's functions theory within the GW approximation and the Bethe−Salpeter equation.[43] These calculations suggest that the energy landscape at D−A interfaces changes considerably depending on the intermolecular interactions present. Due to significant differences in electrostatic interactions and polarization energies, different intermolecular arrangements can result in shifts of the interfacial dipole and CT state energy of several hundred meV. Optical, photoelectron, and electrochemical spectroscopies provide additional support for these findings.[21,44,53−58] Considering both the theoretical and experimental supports for these shifts in energetics at D−A interfaces and in mixed phases relative to the pure materials, combined with their potential impact on the OPV device performance, it is important to identify the molecular factors giving rise to such energetics. Systematically controlling intermolecular interactions and energetics will provide a powerful tool to improve the performance of OPV systems.

Here, four model ADT derivatives that can be thermally evaporated with C_{60} were chosen to investigate the influence of halogenation on the energy landscape at interfaces and in mixed phases in OPV devices (Figure 1). Importantly, each of these
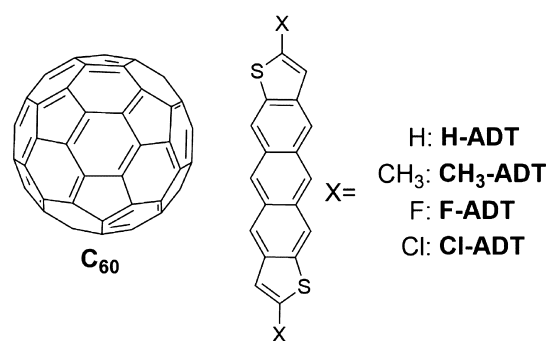
Figure 1. Chemical structures of C_{60} and ADT derivatives used in this work.

derivatives can be thermally evaporated to form well-defined layered structures with known molecular orientations, thus providing the potential for clean interfaces with C_{60} that reduce the number of unknown variables in the systems. To probe the effects of fluorination, and halogenation in general, at levels commonly used in efficient donor polymers (i.e., one to two fluorine atoms per repeat unit), we compare end-substituted ADT derivatives with hydrogen, methyl, fluorine, and chlorine, as depicted in Figure 1. To probe the interfacial energetics between phases of pure materials, we use ultraviolet photoelectron spectroscopy (UPS) during stepwise deposition of C_{60} on top of the varying ADT derivatives, combined with external quantum efficiency (EQE) measurements of the CT states in bilayer PV devices. To probe the energetics in mixed phases, we use UPS measurements of blend films with varying X-ADT:C_{60}
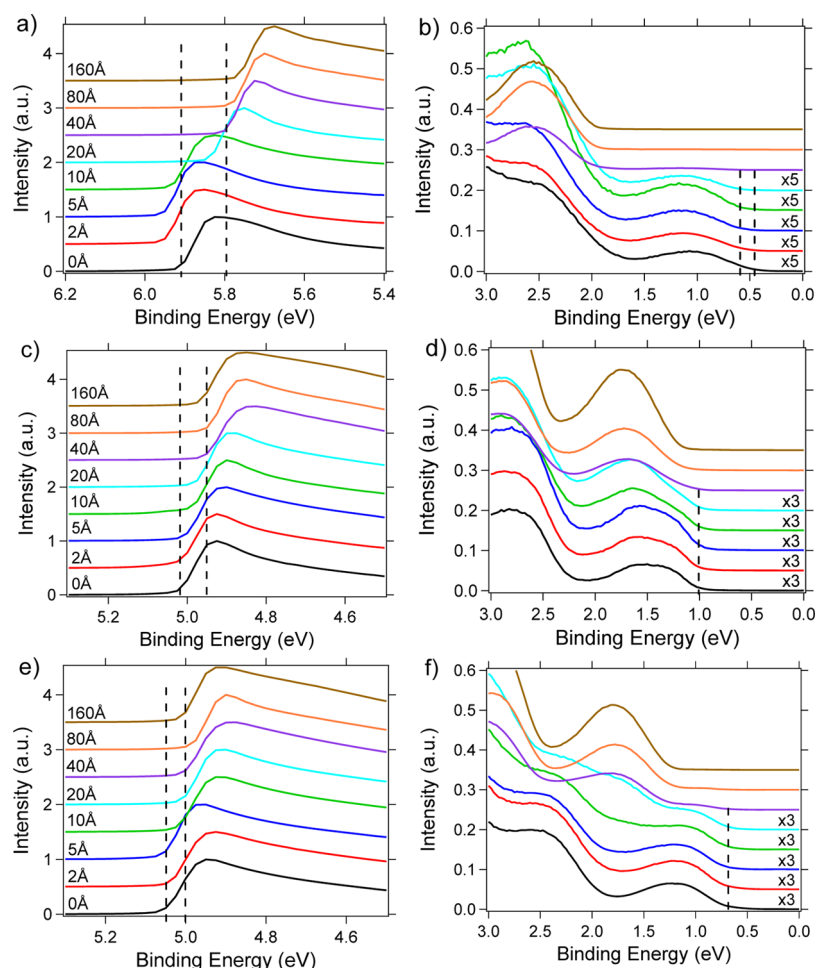
Figure 2. UPS spectra showing the SECO (a,c,e) and HOMO onset (b,d,f) regions for H-ADT/C_{60}, F-ADT/C_{60}, and Cl-ADT/C_{60} bilayers during stepwise C_{60} deposition. The UPS measurements were recorded with an H Lyman-α source emitting at 10.2 eV.[63]

composition and EQE measurements of the CT state energies in PV cells based on these X-ADT:C_{60} blends. To provide molecular-level details, these experimental results are compared with the results from DFT calculations at the optimally tuned (OT)-ωB97X-D/6-31G(d,p) level, where a continuum dielectric (ε = 4.24) is used to represent the majority C_{60} environment of the mixed phase.

■ EXPERIMENTAL SECTION

Materials. PEDOT:PSS (CLEVIOS P VP AI 4083), C_{60} (Nano-C, 99.5%), bathocuproine (BCP, TCI, >99.0%), and Al (99.99%, Angstrom Engineering) were purchased from commercial suppliers and used as received. H-ADT,[59] F-ADT,[60] and CH_3-ADT[61] were synthesized following literature procedures. Synthesis and characterization of the Cl-ADT derivative are reported in the Supporting Information.

Single crystals of Cl-ADT and F-ADT were grown according to previously reported procedures.[60,62] X-ray diffraction data were collected for the crystals using a Bruker X8 PROTEUM (Cu Kα) diffractometer.

Grazing Incidence Wide-Angle X-ray Scattering. Films of Cl-ADT and H-ADT (50 nm thick) were prepared by thermal evaporation at a rate of 0.5 Å/s on silicon wafers with a 300 nm thick oxide layer. Grazing incidence wide-angle X-ray scattering (GIWAXS) measurements were performed at D-line, CHESS at Cornell University. The X-ray beam, with a

wavelength of 1.155 Å and a wide band pass (1.47%), was incident on the films at an angle of 0.15°. A PILATUS 200K detector was placed 90 mm from the sample to record the images.

PV Device Fabrication and Characterization. Patterned indium tin oxide (ITO)-coated glass substrates (Tinwell Tech., 15 Ω/sq) were sequentially sonicated in aqueous detergent (sodium dodecyl sulfate, Sigma-Aldrich), deionized water, acetone, and 2-propanol each for 15 min. After drying with nitrogen, substrates were exposed to UV−ozone treatment for 10 min to remove organic contaminants. PEDOT:PSS was spun-cast at 5000 rpm for 50 s and then annealed on a hot plate at 130 °C for 15 min in air. Anthradithiophenes and C_{60} were thermally evaporated at a typical pressure of 1×10^{-7} mbar. For bilayer devices, 25 nm of X-ADT was deposited at a rate of 0.5 Å/s and 40 nm C_{60} was deposited at a rate of 1 Å/s. For blend films, X-ADT and C_{60} were codeposited at different rates (0.02−1.0 Å/s) to satisfy desired blend ratios with a total thickness of 50 nm. Finally, 10 nm BCP at 0.5 Å/s was deposited, and aluminum (100 nm, 1−3 Å/s) electrodes were evaporated through a shadow mask that defined four cells of 0.1 cm^2 area and four cells of 0.2 cm^2 area per substrate. Solar cell performance was measured using a solar simulator (ABET Technologies, 11002) at 100 mW/cm^2 illumination (AM 1.5G). The intensity was adjusted to 100 mW/cm^2 using a photodiode calibrated with a KG5 filter (ABET Technologies).
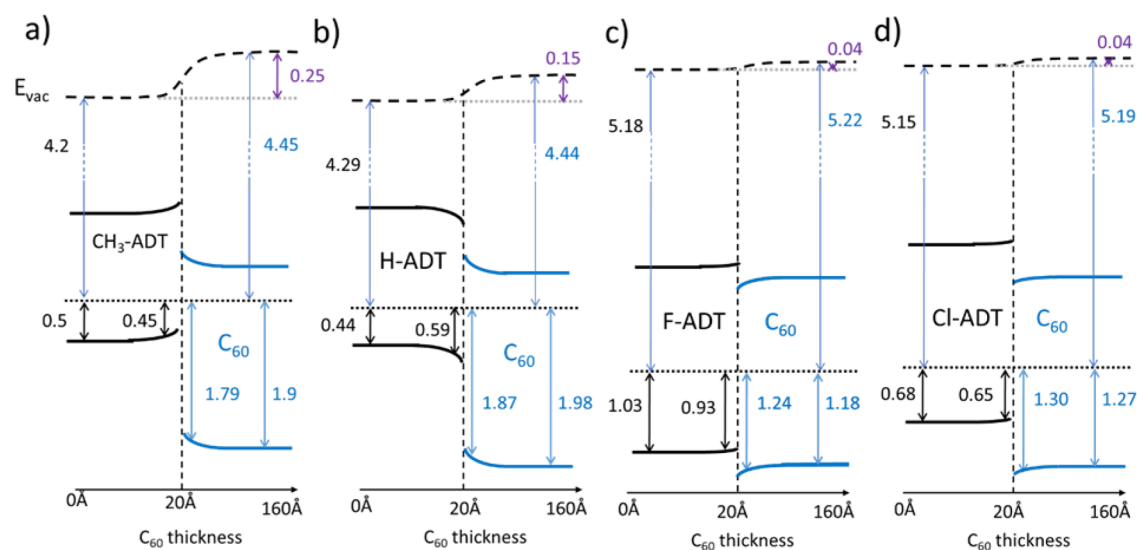
Figure 3. Resulting energy diagrams for CH_3-ADT/C_{60} (a), H-ADT/C_{60} (b), F-ADT/C_{60} (c), and Cl-ADT/C_{60} (d) bilayers during stepwise C_{60} deposition.

Sensitive EQE measurements were taken at short-circuit conditions under focused monochromatic (CM110, Spectral Products) illumination from a 150 W tungsten−halogen light source (ASBN-W, Spectral Products) chopped by an optical chopper (MC2000, Thorlabs) at 84 Hz. Multiple optical filters were used to prevent unwanted light harmonics in the range of PV device absorbance from interfering with the measurement. The current from the PV device was amplified with a current-to-voltage amplifier (RDM-Apps) and further amplified with a lock-in amplifier (SR830, Stanford Research Systems). A calibrated silicon photodiode (FDS100) and a calibrated germanium photodiode (FDG03) purchased from Thorlabs were used to measure the incident light intensity at each wavelength. The uncertainty in the absolute EQE is estimated at ±7% due primarily to the uncertainty associated with the photodiode calibration (±5%), light source intensity fluctuations, and small variations in alignment.

Ultraviolet and X-ray Photoelectron Spectroscopy Measurements. Thin films for UPS were prepared by thermal evaporation on nonpatterned ITO-coated glass substrates (Tinwell Tech., 15 Ω/sq), utilizing procedures similar to those reported for the PV device fabrication. The samples were transferred between the evaporation chamber ($<5 \times 10^{-7}$ mbar) and the UPS analysis chamber ($<1 \times 10^{-9}$ mbar) without breaking vacuum. UPS measurements were taken with an Excitech H Lyman-α photon source (10.2 eV) coupled with a PHI 5600 ultrahigh vacuum system with a hemispherical electron energy analyzer, as detailed in our previous publication.[63] A sample bias of −5 V and a pass energy of 5.85 eV were used for the UPS measurements. The work functions (WFs) of the samples were determined from the equation WF = $h\nu$ − SECO, where $h\nu$ is 10.2 eV and SECO is the secondary electron cutoff. The IEs were determined by the equation IE = WF + HOMO onset. The SECO and IE of the samples were determined by the intersection of the background and a linear fit to the lower 50% of the SECO or highest occupied molecular orbital (HOMO) peak. Uncertainties in IEs based on spot-to-spot and sample-to-sample variations are ±0.05 eV.

DFT Calculations. DFT calculations were carried out using the Gaussian 09 rev. E.01 suite at the optimally tuned OT-

ωB97X-D/6-31G(d,p) level. Omega tuning was carried out via nonempirical gap tuning of monomers for each ADT of interest and C_{60} that were geometry-optimized at the ωB97X-D/6-31G(d,p) level. The final ω value was obtained as an average over this set. ω values ranged from 0.1538 to 0.1754 $bohr^{-1}$, with a final value of 0.1637 $bohr^{-1}$ being used in the calculations; using a single ω for all molecular and complex calculations allows us to directly compare molecular orbital energies and state energies across all systems explored. Individual molecular geometries were then reoptimized at this level inside of a diethyl ether polarizable continuum model (PCM) ($\varepsilon = 4.24$) prior to being placed in dimer configurations. All time-dependent (TD) DFT calculations were completed using the PCM with a diethyl ether medium.

Quadrupole Calculations. Molecular quadrupole tensors were determined via the generalized distributed multipole analysis using the GDMA 2.2.11 program.[64] Density matrices used for these analyses were determined at the ωB97xd/6-31G(d,p) level using the Gaussian 09 rev. E.01 program with a default ω value using structures optimized at the same level. An atom-centered approach was used, including all atoms within the respective molecules and multipoles being calculated to the hexadecapole to recreate the molecular electrostatic potential.

■ RESULTS AND DISCUSSION

Interfacial Energetics. The results of the UPS measurements are displayed in Figure 2a−f for the stepwise deposition of C_{60} on H-ADT, F-ADT, and Cl-ADT, and the deposition of C_{60} on CH_3-ADT is shown in Supporting Information Figure S1. The IEs, HOMO onsets versus Fermi energy, and WFs extracted from these measurements are displayed schematically in Figure 3 and quantitatively in Supporting Information Figure S3. Supporting Information Figure S2 shows example UPS spectra demonstrating how both H-ADT and C_{60} IEs were extracted from the H-ADT/C_{60} bilayer spectra. Replacing only the two terminal H atoms on the long axis of the H-ADT molecule with Cl or F atoms results in an increase in the IE of up to nearly 1.5 eV, from ca. 4.7 eV for CH_3-ADT and H-ADT to 5.83 and 6.21 eV for Cl-ADT and F-ADT, respectively. The dramatic increase in the IE between the nonhalogenated and halogenated ADT derivatives is in part attributed to the tip-on
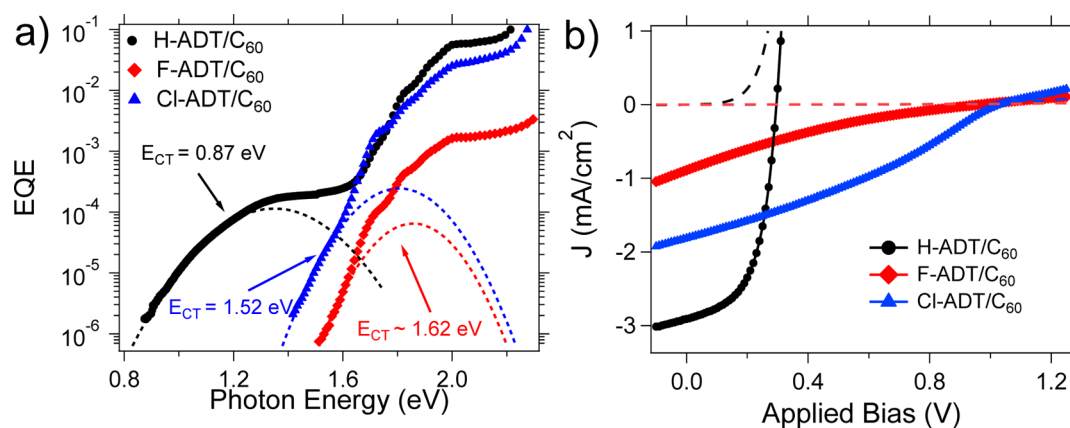
Figure 4. (a) Sensitive EQE of H-ADT/C_{60}, F-ADT/C_{60}, and Cl-ADT/C_{60} bilayer PV devices. The fits to the CT states are shown with dashed lines. (b) Current density vs voltage characteristics in the dark and under AM 1.5G illumination.

orientation of the ADT derivatives on the substrate and the differing quadrupoles (see below) along the long axis of the molecule. These tip-on orientations are confirmed by GIWAXS measurements for H-ADT and Cl-ADT, as displayed in Figure S4; the tip-on orientation of F-ADT was previously reported.[65] Crystal structures, as determined from single-crystal X-ray diffraction measurements and displayed in Figure S5, show that the ADT derivatives all adopt a similar herringbone packing structure with the main variation occurring in d_{001}, which increases from 14.35 Å for H-ADT to 16.82 Å for Cl-ADT.

DFT calculations of the isolated ADT derivatives show that the HOMO of H-ADT lies 0.13 and 0.19 eV higher than the HOMOs of Cl-ADT and F-ADT, respectively. Although this trend does mirror the UPS measurements, the overall difference is greatly reduced; experimentally, we measure differences of 1.1 and 1.48 eV between the IEs of H-ADT and Cl-ADT or F-ADT, respectively. These large differences are most likely explained by the fact that we are comparing gas-phase calculations to macroscopic solid-state experimental measurements. We contend that the significant differences in the molecular quadrupoles, as listed in Table S1, are key factors for the massive difference in the IEs between the CH_3- or H-terminated ADTs and the Cl- or F-terminated ADTs.[66,67] A quintessential example demonstrating the effect of quadrupole sign and resulting surface dipole on the IE is the large (up to 0.6 eV) change in the IE for the same molecule as the molecular orientation changes from edge-on to face-on.[66,68] In our X-ADT series, the long-axis quadrupole along the conjugated core shifts from large and positive for CH_3-ADT (29.55 D-Å) to significantly smaller and positive H-ADT (13.99 D-Å) to increasingly negative for F-ADT (−17.53 D-Å) and Cl-ADT (−21.80 D-Å), indicating that the ends of the molecules shift from positive charge to negative charge. Additionally, we see that the normal component of the quadrupole (i.e., that due to the π-electron cloud) is largely reduced from H-ADT/CH_3-ADT (−23.92/−30.01 D-Å) to F-ADT/Cl-ADT (−8.24/−6.69 D-Å), indicating that the π electron density is being pulled from the conjugated core to the halogenated end groups. Using the trends from our DFT-calculated quadrupoles, the molecular orientations determined by GIWAXS, and the formulas presented in the work by the Koch group,[66,67] we predict that the IEs of H-ADT and CH_3-ADT will be less than those of Cl-ADT and F-ADT based purely on quadrupolar and surface dipole/orientation effects. Alternative models,[69−71] whereby orientation-dependent variations in IEs are attributed primarily

to how molecular orientations affect the polarization energies in thin films without explicitly accounting for surface dipoles, should also predict a lower IE of H-ADT and CH_3-ADT versus Cl-ADT and F-ADT based primarily on the tip-on orientations and quadrupolar interactions.

The UPS results and plots of energy levels presented in Figures 2, 3, and S1−S3 show that the dipole at the X-ADT/C_{60} interface varies as CH_3-ADT > H-ADT > F-ADT = Cl-ADT. Here, the interface dipole is taken as the shift in the WF between the pure X-ADT film and the film with 40 Å C_{60}. In the case of H-ADT, the interface dipole points toward the ADT side, following the convention used in most UPS studies with the interface dipole pointing toward the positive end. Initially, we expected that the interface dipoles at the X-ADT/C_{60} interfaces for F-ADT and Cl-ADT would point in the opposite direction as H-ADT and CH_3-ADT, owing to the greater electronegativity of the F and Cl atoms and the sign change in the long-axis quadrupole component as previously discussed. Instead, we find that there is almost no interface dipole between the halogenated ADTs and C_{60}, and the small 0.04 eV dipole points in the same direction as the CH_3-ADT/C_{60} and H-ADT/C_{60} interface dipoles.

The energy landscapes displayed in Figures 3 and S3 show that the CH_3-ADT/C_{60} and H-ADT/C_{60} interfacial energetics appear more favorable for dissociating interfacial CT states. Here, the HOMO of H-ADT bends away from the Fermi level as C_{60} is deposited. This, combined with the shift in the vacuum level, leads to an increase in the IE of H-ADT from 4.73 eV without C_{60} to 4.96 eV with 20 Å C_{60}. Furthermore, the HOMO of C_{60} bends upward at the interface with H-ADT. Assuming that the lowest unoccupied molecular orbital (LUMO) parallels the HOMO for C_{60}, this upward bending of the HOMO at the interface would mean that the LUMO also bends upward at the interface. Accordingly, it is more energetically favorable for both holes in H-ADT and electrons in C_{60} to move away from the interface. By contrast, for the halogenated ADTs, the energy landscape is nearly flat, with a small amount of unfavorable upward bending of the X-ADT HOMOs and downward bending of the C_{60} LUMO at the interface. Contrary to our expectations, these bilayer studies indicate that halogenation leads to a less favorable energy landscape for charge separation in the halogen-ADT/C_{60} systems. These interfacial energetic shifts most likely arise primarily from a combination of interfacial electrostatic interactions (e.g., quadrupole-induced dipole) and interfacial

disorder. For example, it was shown through both experiment and theoretical calculations that interfacial energetic disorder may contribute to interfacial energetic shifts,[72,73] whereas theoretical calculations have shown how interfacial electrostatic interactions can lead to shifts in energy states at donor–acceptor interfaces.[42,71,74,75]

To further probe interfacial energetics in the materials, we fabricated bilayer OPV devices and utilized sensitive EQE measurements to probe the CT state absorbance, with the EQE and current–voltage characteristics presented in Figure 4. The bilayer OPV results show higher short-circuit current densities (J_{SC}) for the H-ADT/C_{60} devices as compared to the F-ADT/C_{60} and Cl-ADT/C_{60} devices. This increased J_{SC} for H-ADT/C_{60} bilayers is consistent with a more favorable energetic landscape for charge separation. However, because of the number of variables that can influence J_{SC} (e.g., exciton diffusion length, charge-carrier mobilities, absorption coefficients, and CT state dissociation probability), it is not possible to definitively say whether the increased J_{SC} for H-ADT/C_{60} devices arises from the more favorable energetic landscape.

The CT absorbance bands in the EQE spectra are fit with eq 1.[76] Here, E_{CT} is the CT state energy; f is related to the electronic coupling between the molecules in the CT state, the internal quantum efficiency, and the number of CT states; and λ is related to the energetic disorder and the reorganization energy.[76,77] As shown in Figure 4a, the CT state energy of the H-ADT/C_{60} bilayer is 0.87 eV, compared to 1.52 eV for the Cl-ADT/C_{60} bilayer. Only a small edge of the CT state absorbance is evident in the Cl-ADT/C_{60} bilayer, which makes it difficult to accurately determine all fitting parameters. However, regardless of what values of λ and f are used, E_{CT} remains at nearly 1.52 eV, as shown in Figure S6. The F-ADT/C_{60} bilayer CT state is higher in energy than the Cl-ADT/C_{60} CT state, but with most of the CT absorbance buried under the C_{60} absorbance, we cannot accurately quantify E_{CT}.

$$\text{EQE}_{CT} \propto \frac{f}{E\sqrt{4\pi\lambda kT}} \exp\left(\frac{-(E_{CT} + \lambda - E)^2}{4\lambda kT}\right) \qquad (1)$$

Typically, as the CT state primarily involves the HOMO of the donor and LUMO of the acceptor, E_{CT} will vary directly with the IE of the donor if the same acceptor is used. Notably, this is a simplified approximation as it does not account for polarization energy differences between the different donors and C_{60}. On the basis of the pure H-ADT and Cl-ADT IEs, it is predicted that the H-ADT/C_{60} and Cl-ADT/C_{60} CT state energies differ by 1.1 eV, which is 0.45 eV greater than the observed 0.65 eV difference in CT state energies. This discrepancy further supports the interfacial energetic shifts as observed in the UPS measurements. In these UPS measurements, the H-ADT IE increases at the interface with C_{60}, whereas the IE of C_{60} decreases. These changes in interfacial energetics result in a larger energy difference between the H-ADT HOMO and C_{60} LUMO at the interface. On the basis of the HOMO and LUMO levels of H-ADT and C_{60} at a C_{60} thickness of 20 Å, our UPS measurements predict that E_{CT} for H-ADT/C_{60} will be 1.12 eV and E_{CT} for Cl-ADT/C_{60} will be 1.75 eV. With these energetic shifts accounted for, the measured E_{CT} difference of 0.65 eV agrees well with the predicted E_{CT} difference of 0.63 eV. These results highlight the importance of accounting for the interfacial energetics in determining E_{CT}.

To obtain further insights into these CT states, we used TDDFT calculations to evaluate the CT state energies for a tip-on ADT/C_{60} configuration. Our results follow the same general trends observed in the experimental data; H-ADT/C_{60} possesses the lowest E_{CT} of 3.20 eV, whereas F-ADT/C_{60} and Cl-ADT/C_{60} have larger E_{CT}s of 3.49 and 3.61 eV, respectively. The absolute values of these calculated results are significantly higher than the experimentally measured E_{CT} values because of only accounting for a single X-ADT molecule and single C_{60} per configuration. As has previously been demonstrated, expanding the system to include multiple donor and acceptor molecules leads to decreased E_{CT} values through delocalization and polarization effects,[51,78,79] though the trends are not fully consistent within a given computational method for a broad set of materials.

Blend Energetics. Blend PV cells and blend films for UPS measurements were fabricated to further experimentally probe the effects of halogenation on material energetics. Specifically, these measurements were carried out to simulate the mixed phases that are present in BHJ PVs. H-ADT and CH_3-ADT display similar trends in E_{CT} and IE values with varying X-ADT:C_{60} composition, as do F-ADT and Cl-ADT (see Figures 5 and S7–S9 and Table 1). Thus, we primarily focus our

Table 1. Summary of Experimentally Measured CT State Energies, λ, f, and IEs

device/material all	E_{CT}[a] (eV)	λ (eV)	$f \times 10^{-3}$ (eV^2)	IE[b] of X-ADT (eV)	IE[b] of C_{60} (eV)
H-ADT bilayer	0.87	0.5	0.066	4.73	6.42
H-ADT 9:1 blend	1.07	0.5	0.099	4.89	5.94
H-ADT 1:9 blend	1.46	0.1	4.313	5.51	6.37
H-ADT 1:19 blend	1.48	0.16	0.198	5.55	6.475
H-ADT 1:49 blend	1.48	0.17	0.047		6.45
Cl-ADT bilayer	1.52	0.3	0.155	5.83	6.46
Cl-ADT 9:1 blend	1.53	0.25	0.042	5.85	6.61
Cl-ADT 1:9 blend	1.6	0.25	5.85	5.8	6.49
Cl-ADT 1:19 blend	1.4	0.13	0.295	5.54	6.43
Cl-ADT 1:49 blend	1.39	0.18	0.03		6.45
F-ADT bilayer	1.62	0.25	0.035	6.21	6.4
F-ADT 1:19 blend	1.56	0.25	1.479	5.77	6.2
F-ADT 1:49 blend	1.04	0.5	0.002		6.4
CH_3-ADT bilayer	0.89	0.5	0.008	4.7	6.35
CH_3-ADT 9:1	1.05	0.5	0.052		
CH_3-ADT 1:9	1.38	0.18	0.557	5.45	6.41

[a]Uncertainty in E_{CT} is ±0.03 eV. [b]Uncertainty in IEs is ±0.05 eV.

discussion on H-ADT:C_{60} and Cl-ADT:C_{60} blends. The blends were initially fabricated with both donor-rich (9:1 X-ADT:C_{60}) and acceptor-rich (1:9 X-ADT:C_{60}) compositions. As shown by the data in Figures 5 and S8 and Table 1, the H-ADT blends show relatively large changes in IE and E_{CT} between the blends of both compositions and the pure material/bilayers, with the lowest energy states for holes, electrons, and CT states lying in
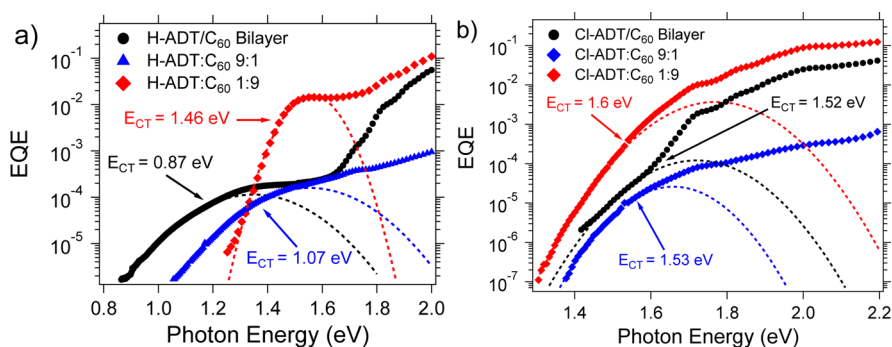
Figure 5. EQE of H-ADT/C_{60} (a) and Cl-ADT/C_{60} (b) bilayers, 9:1, and 1:9 blends, with fits to the CT state component being indicated by dashed lines.
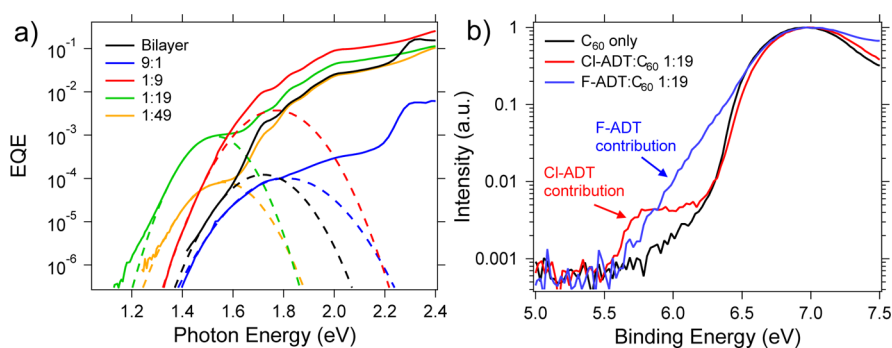

Figure 6. EQE spectra of Cl-ADT:C_{60} blend and bilayer PVs with fits to the CT absorbance band shown (a) and UPS spectra of pure C_{60}, Cl-ADT:C_{60}, and F-ADT:C_{60} blends at a 1:19 ratio (b). In the UPS spectra, the binding energy is referenced to the vacuum level at 0 eV.

the pure H-ADT phase, pure C_{60} phase, and at interfaces between these pure phases, respectively. This trend is in agreement with previous reports, where IEs, oxidation potentials, and CT energies increase in mixed phases,[21,44] whereas the Cl-ADT blends show similar IEs and E_{CT} values in blends of both compositions and the pure materials/bilayers.

In the donor-rich blends with a 9:1 X-ADT:C_{60} ratio by volume, the IE of Cl-ADT remains the same as it is in the pure state (ca. 5.85 eV), whereas the IE of H-ADT increases from 4.73 eV in the pure state to 4.89 eV in the 9:1 blend. More drastically, the IE of C_{60} decreases from 6.42 eV for pure C_{60} to 5.94 eV in the 9:1 H-ADT blend and increases to 6.61 eV in the 9:1 Cl-ADT blend. Qualitatively, these trends are similar to those observed in energetics for the X-ADT/C_{60} bilayer interfaces; that is, the IEs of H-ADT and C_{60} increase and decrease, respectively, at the H-ADT/C_{60} interface, whereas the IE of Cl-ADT and C_{60} show more minimal changes at the Cl-ADT/C_{60} interface. In the acceptor-rich blends with a 1:9 X-ADT:C_{60} ratio, IEs of both Cl-ADT and C_{60} remain close to the values in the pure materials; however, the IE of H-ADT increases by nearly 0.8 eV, to a value of 5.5 eV. These changes in IEs may arise from the expected mixture of ADT orientations now present in the film and the molecular orientation effects on the surface dipole,[66,67] and from the differing polarization energies afforded by the surrounding C_{60} molecules.

To further probe the energetics in the blend materials, we again performed sensitive EQE measurements on the PV cells and fit the CT state region according to eq 1, as shown in Figure 5. The extracted E_{CT} values follow a trend similar to that predicted from the UPS measurements of the IEs. Here, E_{CT} increases from 0.87 to 1.46 eV in going from the H-ADT bilayer to the 1:9 blend, which largely parallels the increasing IE

of H-ADT. Similarly, as the IEs of Cl-ADT and C_{60} varied little between the bilayers and blends, the E_{CT} values for Cl-ADT/C_{60} blends and bilayers display similar E_{CT} values ranging from 1.52 to 1.6 eV.

One explanation for the significant difference in energetics between the H-ADT:C_{60} and Cl-ADT:C_{60} blends is the difference in donor aggregation behavior. For example, one reason that Cl-ADT may remain the same in bilayer and blend films could be that Cl-ADT has a strong tendency to aggregate and form small crystallites. In this case, the energetics of Cl-ADT are likely to be similar between the blends and bilayers. On the other hand, H-ADT may be well-dispersed in the 1:9 blend, thus resulting in a significant change in energetics relative to the pure polycrystalline material. To determine if aggregation is responsible for the nearly constant E_{CT} value in the Cl-ADT:C_{60} blends, we compare the GIWAXS data for H-ADT and Cl-ADT in the 1:9 C_{60} blends, as shown in Supporting Information Figure S4. For both blends, we do not observe any diffraction spots or rings from the ADT derivatives. The diffraction rings that are evident are from C_{60}.[80] However, small clusters of a handful of molecules are likely to be invisible to GIWAXS, but these small aggregates are likely to show different energetic properties than dispersed single molecules. To further examine if small-scale aggregation may occur in the 1:9 Cl-ADT:C_{60} blends, we prepared PV devices with 1:19 and 1:49 ratios. With 19 and 49 times more C_{60} than Cl-ADT (by volume), the Cl-ADT molecules are more likely to be molecularly dispersed in the C_{60} matrix than in the 1:9 blend. Surprisingly, in both higher-ratio Cl-ADT:C_{60} blend devices, a lower energy CT state clearly emerges in the EQE spectrum, as shown in Figure 6a. The most likely explanation for the appearance of this new lower-energy CT state is that Cl-ADT

transitioned from being primarily in small clusters in the 1:9 blend to being primarily molecularly dispersed in the 1:19 and 1:49 blends. The CT state in both blends is 0.13 eV lower than in the bilayer device. To the best of our knowledge, this is the first example where E_{CT} decreases in moving from donor/C_{60} bilayers to blends. To verify that this trend was not unique to Cl-ADT devices, we also prepared blend devices with F-ADT at 1:19 and 1:49 F-ADT:C_{60} ratios. As evident in Figure S9, the 1:49 F-ADT:C_{60} blend shows the appearance of a low-energy CT state at 1.04 eV, which is not apparent in the bilayer devices.

The energetics in the 1:19 and 1:49 blend films with Cl-ADT and F-ADT were further investigated by UPS. In the 1:49 blends, the signal from the ADT derivatives is below our limit of detection, as shown in Figure S10, but in the 1:19 blends, a clear signal from the ADT derivatives is apparent. Figure 6b shows the UPS spectra of these 1:19 blends on a semilog plot, with the spectra shifted by the WFs to put the vacuum levels at 0 eV. In agreement with the EQE measurements of the CT states, both F-ADT and Cl-ADT show lower IEs in these blends with C_{60}. Fitting of these spectra with a linear y-axis shows IEs for F-ADT and Cl-ADT of ca. 5.77 and 5.54 eV, which are 0.44 and 0.29 eV lower than those in the pure F-ADT and Cl-ADT films, respectively. Overall, this combination of CT state measurements and IE measurements clearly shows that both energies are lowered in these dilute X-ADT:C_{60} blends.

We turn again to TDDFT calculations to determine if the opposite trends in E_{CT} in going from bilayers to blends observed for the nonhalogenated and halogenated ADT derivatives may in part arise due to the molecular arrangement of the CT state (tip-on for bilayer vs all orientations present in the blend) and associated electrostatic interactions. In the bilayer systems, GIWAXS shows that Cl-ADT molecules are oriented tip-on with respect to the substrate and deposited C_{60} layer. Although we assume that the CT states are predominantly tip-on for the bilayers based on the GIWAXS measurements, we note that GIWAXS is a bulk measurement and is not specific to molecules at the surface (where the CT states will form) or molecules in amorphous regions. TDDFT results show that the face-on and edge-on orientations have larger CT state oscillator strengths (Table S2), and thus these face-on and edge-on CT complexes are expected to be the dominant contributors to the CT absorbance in the low donor blends. Therefore, the CT absorbance band is viewed as representing the tip-on orientation in the bilayers and the face-on and edge-on orientations for the dilute blends. Looking at the orientation dependence of the CT state energy in H-ADT/C_{60} and Cl-ADT/C_{60} complexes (Figure 7 and Table S2), the calculated E_{CT} values do show a strong dependence on the molecular orientation. However, the dependence of the CT state energy of these dimers alone is insufficient to fully explain the experimental results. For example, the calculated CT state energies of all X-ADT/C_{60} tip-on configurations are 0.71−0.89 eV higher than those for the face-on configurations; yet, experimentally, the tip-on CT states (bilayers) are lower in energy than the face-on CT states (blends) for the CH_3-ADT/C_{60} and H-ADT/C_{60} systems. This disagreement suggests that orientation effects alone cannot explain the observed experimental data. Rather, polarization and delocalization effects due to gross changes in the molecular environments must be accounted for and are likely responsible for the shifts in
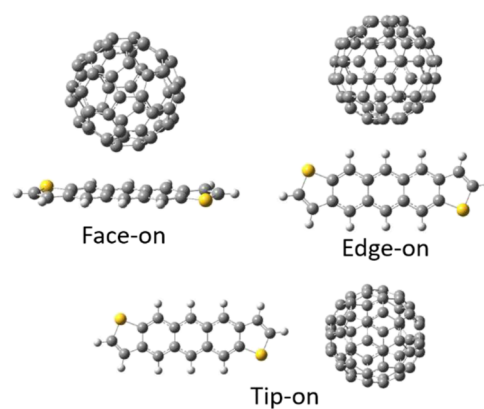

Figure 7. Schematic of the intermolecular orientations investigated in the DFT calculations.

CT energies when comparing the bilayer and blend configurations.

CONCLUSIONS

The dipole at the X-ADT/C_{60} interface does not reverse in direction when the terminal hydrogen atom is substituted by either fluorine or chlorine; rather, this dipole is reduced from 0.15 to 0.04 eV. Whereas previous theoretical calculations indicated more favorable energy landscapes for charge separation when C_{60} is interacting with the more electronegative part of a molecule, our UPS measurements indicate that the energy landscape is more favorable for charge separation when C_{60} is interacting with a more electropositive end group, for example, hydrogen. Furthermore, our measurements of blend material systems indicate that halogenation of ADT molecules can lead to lower CT state energies in the mixed phase relative to at interfaces between pure phases. However, the halogenated compounds appear to have a high propensity to aggregate, with the molecularly dispersed phase only evident at ADT concentrations of around 5% and below. In this ADT material system, the less favorable energy landscape for high PV performance upon halogenation suggests that commonly observed performance improvements in OPV materials upon fluorination are not due to energetics and thus may be attributed more to morphological effects, for example, lower fullerene miscibility in the donor phase and vice versa or a more favorable intermolecular arrangement between donor and acceptor (e.g., face-on).[19] Furthermore, as the energetics will likely vary with molecular orientation, fluorination may lead to more favorable energy landscapes for BHJ PVs if a face-on donor−acceptor orientation is adopted at the interfaces between donor-rich and acceptor-rich domains. Future directions involve seeing if these same trends apply to high-performing fluorinated polymers used in BHJ PVs.

ASSOCIATED CONTENT

Ⓢ Supporting Information

The Supporting Information is available free of charge on the ACS Publications website at DOI: 10.1021/acs.jpcc.7b11729.

> Cl-ADT synthetic details, UPS spectra, plots of IEs and WFs extracted from the UPS data, GIWAXS plots, EQE spectra, crystal structure images for H-ADT, Cl-ADT, and F-ADT, cif figures for Cl-ADT and F-ADT, and calculated quadrupole components, E_{CT} values, and oscillator strengths (PDF)

■ AUTHOR INFORMATION

Corresponding Author

*E-mail: kenneth.graham@uky.edu.

ORCID ⊙

Chad Risko: 0000-0001-9838-5233

John E. Anthony: 0000-0002-8972-1888

Kenneth R. Graham: 0000-0002-6387-3998

Notes

The authors declare no competing financial interest.

■ REFERENCES

(1) Cui, Y.; Yao, H.; Gao, B.; Qin, Y.; Zhang, S.; Yang, B.; He, C.; Xu, B.; Hou, J. Fine-Tuned Photoactive and Interconnection Layers for Achieving over 13% Efficiency in a Fullerene-Free Tandem Organic Solar Cell. *J. Am. Chem. Soc.* **2017**, *139*, 7302−7309.

(2) National Renewable Energy Laboratory. National Center for Photovoltaics. http://www.nrel.gov/ncpv/ (accessed Jan 7, 2016).

(3) Son, H. J.; Wang, W.; Xu, T.; Liang, Y.; Wu, Y.; Li, G.; Yu, L. Synthesis of Fluorinated Polythienothiophene-Co-Benzodithiophenes and Effect of Fluorination on the Photovoltaic Properties. *J. Am. Chem. Soc.* **2011**, *133*, 1885−1894.

(4) Chen, H.-C.; Chen, Y.-H.; Liu, C.-C.; Chien, Y.-C.; Chou, S.-W.; Chou, P.-T. Prominent Short-Circuit Currents of Fluorinated Quinoxaline-Based Copolymer Solar Cells with a Power Conversion Efficiency of 8.0%. *Chem. Mater.* **2012**, *24*, 4766−4772.

(5) Nguyen, T. L.; Choi, H.; Ko, S.-J.; Uddin, M. A.; Walker, B.; Yum, S.; Jeong, J.-E.; Yun, M. H.; Shin, T. J.; Hwang, S.; et al. Semi-Crystalline Photovoltaic Polymers with Efficiency Exceeding 9% in a ~300 nm Thick Conventional Single-Cell Device. *Energy Environ. Sci.* **2014**, *7*, 3040−3051.

(6) Zhao, J.; Li, Y.; Yang, G.; Jiang, K.; Lin, H.; Ade, H.; Ma, W.; Yan, H. Efficient Organic Solar Cells Processed from Hydrocarbon Solvents. *Nat. Energy* **2016**, *1*, 15027.

(7) Bin, H.; Zhang, Z.-G.; Gao, L.; Chen, S.; Zhong, L.; Xue, L.; Yang, C.; Li, Y. Non-Fullerene Polymer Solar Cells Based on Alkylthio and Fluorine Substituted 2D-Conjugated Polymers Reach 9.5% Efficiency. *J. Am. Chem. Soc.* **2016**, *138*, 4657−4664.

(8) Huang, J.; Carpenter, J. H.; Li, C.-Z.; Yu, J.-S.; Ade, H.; Jen, A. K.-Y. Highly Efficient Organic Solar Cells with Improved Vertical Donor-Acceptor Compositional Gradient Via an Inverted Off-Center Spinning Method. *Adv. Mater.* **2016**, *28*, 967−974.

(9) Schroeder, B. C.; Huang, Z.; Ashraf, R. S.; Smith, J.; D'Angelo, P.; Watkins, S. E.; Anthopoulos, T. D.; Durrant, J. R.; McCulloch, I. Silaindacenodithiophene-Based Low Band Gap Polymers - The Effect of Fluorine Substitution on Device Performances and Film Morphologies. *Adv. Funct. Mater.* **2012**, *22*, 1663−1670.

(10) Price, S. C.; Stuart, A. C.; Yang, L.; Zhou, H.; You, W. Fluorine Substituted Conjugated Polymer of Medium Band Gap Yields 7% Efficiency in Polymer-Fullerene Solar Cells. *J. Am. Chem. Soc.* **2011**, *133*, 4625−4631.

(11) Zhou, H.; Yang, L.; Stuart, A. C.; Price, S. C.; Liu, S.; You, W. Development of Fluorinated Benzothiadiazole as a Structural Unit for a Polymer Solar Cell of 7 % Efficiency. *Angew. Chem., Int. Ed.* **2011**, *50*, 2995−2998.

(12) Carsten, B.; Szarko, J. M.; Son, H. J.; Wang, W.; Lu, L.; He, F.; Rolczynski, B. S.; Lou, S. J.; Chen, L. X.; Yu, L. Examining the Effect of the Dipole Moment on Charge Separation in Donor-Acceptor Polymers for Organic Photovoltaic Applications. *J. Am. Chem. Soc.* **2011**, *133*, 20468−20475.

(13) Chen, H.-Y.; Hou, J.; Zhang, S.; Liang, Y.; Yang, G.; Yang, Y.; Yu, L.; Wu, Y.; Li, G. Polymer Solar Cells with Enhanced Open-Circuit Voltage and Efficiency. *Nat. Photonics* **2009**, *3*, 649−653.

(14) Liu, P.; Zhang, K.; Liu, F.; Jin, Y.; Liu, S.; Russell, T. P.; Yip, H.-L.; Huang, F.; Cao, Y. Effect of Fluorine Content in Thienothiophene-Benzodithiophene Copolymers on the Morphology and Performance of Polymer Solar Cells. *Chem. Mater.* **2014**, *26*, 3009−3017.

(15) Tumbleston, J. R.; Stuart, A. C.; Gann, E.; You, W.; Ade, H. Fluorinated Polymer Yields High Organic Solar Cell Performance for a Wide Range of Morphologies. *Adv. Funct. Mater.* **2013**, *23*, 3463−3470.

(16) Jiang, B.; Du, C. C.; Li, M. J.; Gao, K.; Kou, L.; Chen, M.; Liu, F.; Russell, T. P.; Wang, H. Synthesis of Fluorinated Diphenyl-Diketopyrrolopyrrole Derivatives as New Building Blocks for Conjugated Copolymers. *Polym. Chem.* **2016**, *7*, 3311−3324.

(17) Do, K.; Saleem, Q.; Ravva, M. K.; Cruciani, F.; Kan, Z.; Wolf, J.; Hansen, M. R.; Beaujuge, P. M.; Brédas, J.-L. Impact of Fluorine Substituents on π-Conjugated Polymer Main-Chain Conformations, Packing, and Electronic Couplings. *Adv. Mater.* **2016**, *28*, 8197−8205.

(18) Zhao, F.; Dai, S.; Wu, Y.; Zhang, Q.; Wang, J.; Jiang, L.; Ling, Q.; Wei, Z.; Ma, W.; You, W.; et al. Single-Junction Binary-Blend Nonfullerene Polymer Solar Cells with 12.1% Efficiency. *Adv. Mater.* **2017**, *29*, 1700144.

(19) Tumbleston, J. R.; Collins, B. A.; Yang, L.; Stuart, A. C.; Gann, E.; Ma, W.; You, W.; Ade, H. The Influence of Molecular Orientation on Organic Bulk Heterojunction Solar Cells. *Nat. Photonics* **2014**, *8*, 385−391.

(20) Calvo-Castro, J.; Morris, G.; Kennedy, A. R.; McHugh, C. J. Effects of Fluorine Substitution on the Intermolecular Interactions, Energetics, and Packing Behavior of N-Benzyl Substituted Diketo-pyrrolopyrroles. *Cryst. Growth Des.* **2016**, *16*, 2371−2384.

(21) Sweetnam, S.; Graham, K. R.; Ndjawa, G. O. N.; Heumüller, T.; Bartelt, J. A.; Burke, T. M.; Li, W.; You, W.; Amassian, A.; McGehee, M. D. Characterization of the Polymer Energy Landscape in Polymer:Fullerene Bulk Heterojunctions with Pure and Mixed Phases. *J. Am. Chem. Soc.* **2014**, *136*, 14078−14088.

(22) Burke, T. M.; McGehee, M. D. How High Local Charge Carrier Mobility and an Energy Cascade in a Three-Phase Bulk Hetero-junction Enable >90% Quantum Efficiency. *Adv. Mater.* **2014**, *26*, 1923−1928.

(23) Chen, W.; Qi, D.-C.; Huang, H.; Gao, X.; Wee, A. T. S. Organic-Organic Heterojunction Interfaces: Effect of Molecular Orientation. *Adv. Funct. Mater.* **2011**, *21*, 410−424.

(24) Yang, P.; Yuan, M.; Zeigler, D. F.; Watkins, S. E.; Lee, J. A.; Luscombe, C. K. Influence of Fluorine Substituents on the Film Dielectric Constant and Open-Circuit Voltage in Organic Photo-voltaics. *J. Mater. Chem. C* **2014**, *2*, 3278−3284.

(25) Carsten, B.; Szarko, J. M.; Lu, L.; Son, H. J.; He, F.; Botros, Y. Y.; Chen, L. X.; Yu, L. Mediating Solar Cell Performance by Controlling the Internal Dipole Change in Organic Photovoltaic Polymers. *Macromolecules* **2012**, *45*, 6390−6395.

(26) McGarry, K. A.; Xie, W.; Sutton, C.; Risko, C.; Wu, Y.; Young, V. G.; Brédas, J.-L.; Frisbie, C. D.; Douglas, C. J. Rubrene-Based Single-Crystal Organic Semiconductors: Synthesis, Electronic Structure, and Charge-Transport Properties. *Chem. Mater.* **2013**, *25*, 2254−2263.

(27) Tada, A.; Geng, Y.; Wei, Q.; Hashimoto, K.; Tajima, K. Tailoring Organic Heterojunction Interfaces in Bilayer Polymer Photovoltaic Devices. *Nat. Mater.* **2011**, *10*, 450−455.

(28) Nakano, K.; Tajima, K. Organic Planar Heterojunctions: From Models for Interfaces in Bulk Heterojunctions to High-Performance Solar Cells. *Adv. Mater.* **2017**, *29*, 1603269.

(29) Verstappen, P.; Kesters, J.; Vanormelingen, W.; Heintges, G. H. L.; Drijkoningen, J.; Vangerven, T.; Marin, L.; Koudjina, S.; Champagne, B.; Manca, J.; et al. Fluorination as an Effective Tool to Increase the Open-Circuit Voltage and Charge Carrier Mobility of Organic Solar Cells Based on Poly(cyclopenta[2,1-b:3,4-B′]-dithiophene-*alt*-quinoxaline) Copolymers. *J. Mater. Chem. A* **2015**, *3*, 2960−2970.

(30) Gélinas, S.; Rao, A.; Kumar, A.; Smith, S. L.; Chin, A. W.; Clark, J.; van der Poll, T. S.; Bazan, G. C.; Friend, R. H. Ultrafast Long-Range Charge Separation in Organic Semiconductor Photovoltaic Diodes. *Science* **2014**, *343*, 512−516.

(31) Lin, Y. L.; Fusella, M. A.; Rand, B. P. The Impact of Local Morphology on Organic Donor/Acceptor Charge Transfer States. *Adv. Energy Mater.* **2018**, 1702816.

(32) Bernardo, B.; Cheyns, D.; Verreet, B.; Schaller, R. D.; Rand, B. P.; Giebink, N. C. Delocalization and Dielectric Screening of Charge Transfer States in Organic Photovoltaic Cells. *Nat. Commun.* **2014**, *5*, 3245.

(33) Groves, C. Suppression of Geminate Charge Recombination in Organic Photovoltaic Devices with a Cascaded Energy Heterojunction. *Energy Environ. Sci.* **2013**, *6*, 1546.

(34) Kipp, D.; Ganesan, V. Exploiting the Combined Influence of Morphology and Energy Cascades in Ternary Blend Organic Solar Cells Based on Block Copolymer Additives. *Macromolecules* **2016**, *49*, 5137−5144.

(35) D'Avino, G.; Mothy, S.; Muccioli, L.; Zannoni, C.; Wang, L.; Cornil, J.; Beljonne, D.; Castet, F. Energetics of Electron−Hole Separation at P3HT/PCBM Heterojunctions. *J. Phys. Chem. C* **2013**, *117*, 12981−12990.

(36) Few, S.; Frost, J. M.; Nelson, J. Models of Charge Pair Generation in Organic Solar Cells. *Phys. Chem. Chem. Phys.* **2015**, *17*, 2311−2325.

(37) Linares, M.; Beljonne, D.; Cornil, J.; Lancaster, K.; Brédas, J.-L.; Verlaak, S.; Mityashin, A.; Heremans, P.; Fuchs, A.; Lennartz, C.; et al. On the Interface Dipole at the Pentacene−Fullerene Heterojunction: A Theoretical Study. *J. Phys. Chem. C* **2010**, *114*, 3215−3224.

(38) Verlaak, S.; Beljonne, D.; Cheyns, D.; Rolin, C.; Linares, M.; Castet, F.; Cornil, J.; Heremans, P. Electronic Structure and Geminate Pair Energetics at Organic-Organic Interfaces: The Case of Pentacene/C_{60} Heterojunctions. *Adv. Funct. Mater.* **2009**, *19*, 3809−3814.

(39) Yost, S. R.; Van Voorhis, T. Electrostatic Effects at Organic Semiconductor Interfaces: A Mechanism for "Cold" Exciton Breakup. *J. Phys. Chem. C* **2013**, *117*, 5617−5625.

(40) Few, S.; Frost, J. M.; Kirkpatrick, J.; Nelson, J. Influence of Chemical Structure on the Charge Transfer State Spectrum of a Polymer:Fullerene Complex. *J. Phys. Chem. C* **2014**, *118*, 8253−8261.

(41) Ryno, S. M.; Risko, C.; Brédas, J.-L. Impact of Molecular Orientation and Packing Density on Electronic Polarization in the Bulk and at Surfaces of Organic Semiconductors. *ACS Appl. Mater. Interfaces* **2016**, *8*, 14053−14062.

(42) Ryno, S. M.; Fu, Y.-T.; Risko, C.; Brédas, J.-L. Polarization Energies at Organic−Organic Interfaces: Impact on the Charge Separation Barrier at Donor−Acceptor Interfaces in Organic Solar Cells. *ACS Appl. Mater. Interfaces* **2016**, *8*, 15524−15534.

(43) Baumeier, B.; Andrienko, D.; Rohlfing, M. Frenkel and Charge-Transfer Excitations in Donor−Acceptor Complexes from Many-Body Green's Functions Theory. *J. Chem. Theory Comput.* **2012**, *8*, 2790−2795.

(44) Graham, K. R.; Ndjawa, G. O. N.; Conron, S. M.; Munir, R.; Vandewal, K.; Chen, J. J.; Sweetnam, S.; Thompson, M. E.; Salleo, A.; McGehee, M. D.; et al. The Roles of Structural Order and Intermolecular Interactions in Determining Ionization Energies and Charge-Transfer State Energies in Organic Semiconductors. *Adv. Energy Mater.* **2016**, *6*, 1601211.

(45) Westacott, P.; Tumbleston, J. R.; Shoaee, S.; Fearn, S.; Bannock, J. H.; Gilchrist, J. B.; Heutz, S.; deMello, J.; Heeney, M.; Ade, H.; et al.

On the Role of Intermixed Phases in Organic Photovoltaic Blends. *Energy Environ. Sci.* **2013**, *6*, 2756.

(46) Shoaee, S.; Clarke, T. M.; Huang, C.; Barlow, S.; Marder, S. R.; Heeney, M.; McCulloch, I.; Durrant, J. R. Acceptor Energy Level Control of Charge Photogeneration in Organic Donor/Acceptor Blends. *J. Am. Chem. Soc.* **2010**, *132*, 12919−12926.

(47) Endres, J.; Pelczer, I.; Rand, B. P.; Kahn, A. Determination of Energy Level Alignment within an Energy Cascade Organic Solar Cell. *Chem. Mater.* **2016**, *28*, 794−801.

(48) Schlenker, C. W.; Barlier, V. S.; Chin, S. W.; Whited, M. T.; McAnally, R. E.; Forrest, S. R.; Thompson, M. E. Cascade Organic Solar Cells. *Chem. Mater.* **2011**, *23*, 4132−4140.

(49) Stevens, M. A.; Arango, A. C. Open-Circuit Voltage Exceeding the Outermost HOMO-LUMO Offset in Cascade Organic Solar Cells. *Org. Electron.* **2016**, *37*, 80−84.

(50) Jakowetz, A. C.; Böhm, M. L.; Sadhanala, A.; Huettner, S.; Rao, A.; Friend, R. H. Visualizing Excitations at Buried Heterojunctions in Organic Semiconductor Blends. *Nat. Mater.* **2017**, *16*, 551−557.

(51) Zheng, Z.; Tummala, N. R.; Fu, Y.-T.; Coropceanu, V.; Brédas, J.-L. Charge-Transfer States in Organic Solar Cells: Understanding the Impact of Polarization, Delocalization, and Disorder. *ACS Appl. Mater. Interfaces* **2017**, *9*, 18095−18102.

(52) Sini, G.; Schubert, M.; Risko, C.; Roland, S.; Lee, O. P.; Chen, Z.; Richter, T. V.; Dolfen, D.; Coropceanu, V.; Ludwigs, S.; et al. On the Molecular Origin of Charge Separation at the Donor-Acceptor Interface. *Adv. Energy Mater.* **2018**, 1702232.

(53) Shoaee, S.; Subramaniyan, S.; Xin, H.; Keiderling, C.; Tuladhar, P. S.; Jamieson, F.; Jenekhe, S. A.; Durrant, J. R. Charge Photogeneration for a Series of Thiazolo-Thiazole Donor Polymers Blended with the Fullerene Electron Acceptors PCBM and ICBA. *Adv. Funct. Mater.* **2013**, *23*, 3286−3298.

(54) Akaike, K.; Kanai, K.; Ouchi, Y.; Seki, K. Influence of Ionization Energy Change on Valence Band Offset in Organic p-n Junction. *Appl. Phys. Lett.* **2009**, *95*, 113306.

(55) Tang, J. X.; Zhou, Y. C.; Liu, Z. T.; Lee, C. S.; Lee, S. T. Interfacial Electronic Structures in an Organic Double-Heterostructure Photovoltaic Cell. *Appl. Phys. Lett.* **2008**, *93*, 043512.

(56) Brumbach, M.; Placencia, D.; Armstrong, N. R. Titanyl Phthalocyanine/C_{60} Heterojunctions: Band-Edge Offsets and Photovoltaic Device Performance. *J. Phys. Chem. C* **2008**, *112*, 3142−3151.

(57) Lau, K. M.; Tang, J. X.; Sun, H. Y.; Lee, C. S.; Lee, S. T.; Yan, D. Interfacial Electronic Structure of Copper Phthalocyanine and Copper Hexadecafluorophthalocyanine Studied by Photoemission. *Appl. Phys. Lett.* **2006**, *88*, 173513.

(58) Ran, N. A.; Roland, S.; Love, J. A.; Savikhin, V.; Takacs, C. J.; Fu, Y.-T.; Li, H.; Coropceanu, V.; Liu, X.; Brédas, J.-L.; et al. Impact of Interfacial Molecular Orientation on Radiative Recombination and Charge Generation Efficiency. *Nat. Commun.* **2017**, *8*, 79.

(59) Laquindanum, J. G.; Katz, H. E.; Lovinger, A. J. Synthesis, Morphology, and Field-Effect Mobility of Anthradithiophenes. *J. Am. Chem. Soc.* **1998**, *120*, 664−672.

(60) Yong, C. K.; Musser, A. J.; Bayliss, S. L.; Lukman, S.; Tamura, H.; Bubnova, O.; Hallani, R. K.; Meneau, A.; Resel, R.; Maruyama, M.; et al. The Entangled Triplet Pair State in Acene and Heteroacene Materials. *Nat. Commun.* **2017**, *8*, 15953.

(61) Chen, M.-C.; Kim, C.; Chen, S.-Y.; Chiang, Y.-J.; Chung, M.-C.; Facchetti, A.; Marks, T. J. Functionalized Anthradithiophenes for Organic Field-Effect Transistors. *J. Mater. Chem.* **2008**, *18*, 1029.

(62) Yamao, T.; Shimizu, Y.; Terasaki, K.; Hotta, S. Organic Light-Emitting Field-Effect Transistors Operated by Alternating-Current Gate Voltages. *Adv. Mater.* **2008**, *20*, 4109−4112.

(63) Boehm, A. M.; Wieser, J.; Butrouna, K.; Graham, K. R. A New Photon Source for Ultraviolet Photoelectron Spectroscopy of Organic and Other Damage-Prone Materials. *Org. Electron.* **2017**, *41*, 9−16.

(64) Stone, A. J. Distributed Multipole Analysis: Stability for Large Basis Sets. *J. Chem. Theory Comput.* **2005**, *1*, 1128−1132.

(65) Storzer, T.; Hinderhofer, A.; Zeiser, C.; Novák, J.; Fišer, Z.; Belova, V.; Reisz, B.; Maiti, S.; Duva, G.; Hallani, R. K.; et al. Growth,

Structure, and Anisotropic Optical Properties of Difluoro-Anthradithiophene Thin Films. *J. Phys. Chem. C* **2017**, *121*, 21011−21017.

(66) Duhm, S.; Heimel, G.; Salzmann, I.; Glowatzki, H.; Johnson, R. L.; Vollmer, A.; Rabe, J. P.; Koch, N. Orientation-Dependent Ionization Energies and Interface Dipoles in Ordered Molecular Assemblies. *Nat. Mater.* **2008**, *7*, 326−332.

(67) Heimel, G.; Salzmann, I.; Duhm, S.; Rabe, J. P.; Koch, N. Intrinsic Surface Dipoles Control the Energy Levels of Conjugated Polymers. *Adv. Funct. Mater.* **2009**, *19*, 3874−3879.

(68) Chen, W.; Qi, D.-C.; Huang, H.; Gao, X.; Wee, A. T. S. Organic-Organic Heterojunction Interfaces: Effect of Molecular Orientation. *Adv. Funct. Mater.* **2011**, *21*, 410−424.

(69) Yoshida, H.; Yamada, K.; Tsutsumi, J.; Sato, N. Complete Description of Ionization Energy and Electron Affinity in Organic Solids: Determining Contributions from Electronic Polarization, Energy Band Dispersion, and Molecular Orientation. *Phys. Rev. B: Condens. Matter Mater. Phys.* **2015**, *92*, 075145.

(70) Topham, B. J.; Soos, Z. G. Ionization in Organic Thin Films: Electrostatic Potential, Electronic Polarization, and Dopants in Pentacene Films. *Phys. Rev. B: Condens. Matter Mater. Phys.* **2011**, *84*, 165405.

(71) Poelking, C.; Tietze, M.; Elschner, C.; Olthof, S.; Hertel, D.; Baumeier, B.; Würthner, F.; Meerholz, K.; Leo, K.; Andrienko, D. Impact of Mesoscale Order on Open-Circuit Voltage in Organic Solar Cells. *Nat. Mater.* **2015**, *14*, 434−439.

(72) Akaike, K.; Koch, N.; Heimel, G.; Oehzelt, M. The Impact of Disorder on the Energy Level Alignment at Molecular Donor-Acceptor Interfaces. *Adv. Mater. Interfaces* **2015**, *2*, 1500232.

(73) Ndjawa, G. O. N.; Graham, K. R.; Li, R.; Conron, S. M.; Erwin, P.; Chou, K. W.; Burkhard, G. F.; Zhao, K.; Hoke, E. T.; Thompson, M. E.; et al. Impact of Molecular Orientation and Spontaneous Interfacial Mixing on the Performance of Organic Solar Cells. *Chem. Mater.* **2015**, *27*, 5597−5604.

(74) D'Avino, G.; Muccioli, L.; Castet, F.; Poelking, C.; Andrienko, D.; Soos, Z. G.; Cornil, J.; Beljonne, D. Electrostatic Phenomena in Organic Semiconductors: Fundamentals and Implications for Photovoltaics. *J. Phys.: Condens. Matter* **2016**, *28*, 433002.

(75) Idé, J.; Mothy, S.; Savoyant, A.; Fritsch, A.; Aurel, P.; Méreau, R.; Ducasse, L.; Cornil, J.; Beljonne, D.; Castet, F. Interfacial Dipole and Band Bending in Model Pentacene/C_{60} Heterojunctions. *Int. J. Quantum Chem.* **2013**, *113*, 580−584.

(76) Vandewal, K.; Tvingstedt, K.; Gadisa, A.; Inganäs, O.; Manca, J. V. Relating the Open-Circuit Voltage to Interface Molecular Properties of Donor:Acceptor Bulk Heterojunction Solar Cells. *Phys. Rev. B: Condens. Matter Mater. Phys.* **2010**, *81*, 125204.

(77) Burke, T. M.; Sweetnam, S.; Vandewal, K.; McGehee, M. D. Beyond Langevin Recombination: How Equilibrium between Free Carriers and Charge Transfer States Determines the Open-Circuit Voltage of Organic Solar Cells. *Adv. Energy Mater.* **2015**, *5*, 1500123.

(78) Yang, B.; Yi, Y.; Zhang, C.-R.; Aziz, S. G.; Coropceanu, V.; Brédas, J.-L. Impact of Electron Delocalization on the Nature of the Charge-Transfer States in Model Pentacene/C_{60} Interfaces: A Density Functional Theory Study. *J. Phys. Chem. C* **2014**, *118*, 27648−27656.

(79) Chen, X.-K.; Ravva, M. K.; Li, H.; Ryno, S. M.; Brédas, J.-L. Effect of Molecular Packing and Charge Delocalization on the Nonradiative Recombination of Charge-Transfer States in Organic Solar Cells. *Adv. Energy Mater.* **2016**, *6*, 1601325.

(80) Elschner, C.; Levin, A. A.; Wilde, L.; Grenzer, J.; Schroer, C.; Leo, K.; Riede, M. Determining the C_{60} Molecular Arrangement in Thin Films by Means of X-Ray Diffraction. *J. Appl. Crystallogr.* **2011**, *44*, 983−990.